

Article

# New Multifunctional Isolated Microinverter with Integrated Energy Storage System for PV Applications

Luis A. M. Barros <sup>\*</sup>, Mohamed Tanta , Tiago J. C. Sousa, Joao L. Afonso  and J. G. Pinto 

Centro ALGORITMI, Universidade do Minho, 4800 Guimarães, Portugal; mtanta@dei.uminho.pt (M.T.); tsousa@dei.uminho.pt (T.J.C.S.); jla@dei.uminho.pt (J.L.A.); gpinto@dei.uminho.pt (J.G.P.)

<sup>\*</sup> Correspondence: lbarros@dei.uminho.pt

Received: 1 July 2020; Accepted: 1 August 2020; Published: 4 August 2020



**Abstract:** This paper proposes a novel multifunctional isolated microinverter which is able to extract the maximum available power from a solar photovoltaic module and inject it into the power grid, while simultaneously charging a battery energy storage system (BESS). The proposed microinverter integrates a novel DC–DC power converter and a conventional DC–AC power converter. The DC–DC power converter is able to send electrical energy to the secondary side of a high-frequency transformer and to the BESS, using only two power switches. Throughout this paper, the converter topology, the operation modes, the control algorithms, and the development of a laboratory prototype of the proposed microinverter are described in detail. Moreover, simulation and experimental results are presented to demonstrate the feasibility of the proposed solution.

**Keywords:** battery energy storage system; microinverter; MPPT; photovoltaic; push–pull power converter

## 1. Introduction

Microinverters are compact power converters that are connected to single solar photovoltaic (PV) modules, with the main purpose of extracting the maximum power from each solar PV module and injecting it into the power grid. Considering that a solar PV module is not an ideal system, where external factors such as the temperature and the radiation influence the available power in the solar PV cells, each microinverter has a control algorithm, called maximum power point tracker (MPPT). The MPPT control algorithm is responsible for accurately tracking the maximum power point (MPP) and continuously maintaining the power converter operating at this point, consequently maximizing the energy produced by the solar PV module. The connection of each microinverter to each solar PV module enables the highest power extraction from each solar PV module, without the influence of the adjacent solar PV modules. This is important to mitigate the shadow effect that gives rise to different local MPP when different solar PV modules of a set are exposed to shadows. Since the microinverter is connected directly to each solar PV module, this effect is attenuated, converting each local MPP as the general MPP [1]. Additionally, these compact power converters enable a modular installation and expansion, without resizing the conventional central inverter [2]. However, microinverters represent a higher initial investment and generally only allow the injection of energy into the power grid. In this case, and by considering a residential solar PV application, having only this operation mode is not very interesting when compared to the possibility of storing energy for later utilization, increasing the flexibility of the installation. The addition of an energy storage system (ESS) would increase the revenue of the owner, particularly in periods when there is no energy consumption, and the injection of energy into the power grid does not pay financially.

The most common microinverters are constituted by a DC–DC power converter followed by a DC–AC power converter. The DC–DC power converter integrates an MPPT algorithm and is

responsible for ensuring a DC-link voltage higher than the peak value of the power grid voltage, usually taking advantage of high-frequency step-up transformers for this purpose. The DC–AC converter is responsible for injecting energy into the power grid, with the full-bridge converter topology being the most common for this purpose. On the other hand, the DC–DC power converter can be implemented with different topologies. The flyback power converter is the most common one, although it is susceptible to core saturation and does not enable continuous power extraction from the solar PV module [3,4]. In order to solve both of these problems, a current-fed push–pull power converter is proposed in [5]. Additionally, this power converter topology allows a simplified drive circuit (since both of the power switches are referenced to the ground), when compared with the full-bridge converter [6] or the half-bridge converter [7] topologies. In [8], a different power converter configuration is presented, in which the microinverter is composed by an interleaved boost converter, a full-bridge converter and a voltage doubler. In order to minimize the large high-frequency turn ratio and thus large leakage inductance from the flyback conventional topology, a hybrid boost–flyback/flyback transformer solution is proposed in [9]. In [10], a new control strategy to improve the efficiency of an interleaved flyback microinverter is presented. Taking into account that a solar PV installation is characterized by low maintenance, it is expected that the power electronics equipment will also have a long lifetime. In that regard, in [11], special importance is given to the lifetime of the electrolytic capacitors that are normally used in the DC-link, presenting a solution based on a DC–AC current source inverter topology. Additionally, an auxiliary decoupling circuit is presented in order to mitigate the double-line frequency ripple in the DC-link voltage. A three-phase 400 W microinverter with low storage capacitance in the DC-link, in order to increase the reliability of the microinverter, is presented in [12]. A single-phase transformerless microinverter solution is presented in [13], and a high-gain step-up with the feature of mitigating the high-frequency common-mode leakage current, as well as reducing the decoupling capacitance, is presented in [14]. Another transformerless approach is presented in [15], where a modular microinverter is presented, which can operate with single or double inputs in order to obtain an adjustable voltage gain and, therefore, be used worldwide regardless of the power grid voltage. In [16–18], an overview of different topologies used in microinverter applications is presented, analyzing and comparing advantages and disadvantages, efficiency, and reliability among them.

Generically, all the presented topologies only enable the injection of energy from the solar PV modules into the power grid. However, there are some emerging innovative topologies with a third stage to interface with a battery energy storage system (BESS). In [19], a new topology with bidirectional energy flow between a nanogrid, a solar PV module and an integrated “short-term storage” is proposed. A bidirectional multiport microinverter is presented in [20], where three full-bridges to interface the different stages (solar PV module, BESS, and power grid) are used with the possibility to operate in stand-alone mode, and in [21] a similar topology is presented. Despite the significant complexity of these power converter topologies, the analysis of these works leads to a main conclusion that the functionalities of the microinverters are in continuous improvement.

Despite the prominent technological developments, the legislation for the exploitation of renewable energy sources has also been changed in order to allow the gradual integration of other renewable energy sources into the power grid. An example of this is the Portuguese legislation, where for up to 200 Wp of solar PV modules, no energy exploration process is necessary. However, the surplus energy produced is injected into the power grid without any financial compensation. In this way, the creation of an ESS becomes an asset for the users, in order to produce and consume their own energy (prosumers). Thus, the microinverter needs an independent control capable of always extracting the maximum power from the solar PV modules and injecting it at the point of consumption for direct usage, existing as the surplus of energy stored for hours without solar production.

Considering all of the aforementioned factors, the main contributions of this paper are: (A) presenting an innovative multifunctional isolated microinverter with a BESS interface; (B) presenting advanced operation modes for the microinverter topology; (C) maintaining a simple hardware structure

of the microinverter topology. The proposed multifunctional isolated microinverter uses only two controlled semiconductors to extract the maximum power from the PV module, to charge a BESS, and to transmit electric energy to the secondary side of a high-frequency power transformer, then, injecting this electric energy into the single-phase power grid.

The rest of the paper is organized as follows: Section 2 describes the proposed multifunctional topology, specifying the available operation modes and the principle of operation of the isolated microinverter; Section 3 describes all the control algorithms necessary for the operation of the multifunctional isolated microinverter (the MPPT control algorithm, the BESS charging control algorithm, the DC-link voltage control and the current control algorithms); Section 4 shows the simulation results in order to validate the performance of the proposed topology; Section 5 describes the operating conditions of the multifunctional isolated microinverter, as well as all the hardware development; Section 6 shows the experimental results of the multifunctional isolated microinverter; finally, in Section 7, the main conclusions are presented, as well as some suggestions for future work.

## 2. Proposed Multifunctional Isolated Topology

The proposed multifunctional high-frequency push–pull topology with galvanic isolation, shown in Figure 1a, presents different and attractive advantages. Besides the inherent advantages of the conventional current-fed push–pull converter, with a simple drive circuit, continuous power extraction from the solar PV modules, and a reduced probability of core saturation, this new topology also does not need a third converter to interface the BESS. By adding a diode,  $D_5$ , a capacitor,  $C_3$ , and implementing a specific control algorithm, the DC–DC power converter is able to send energy to the secondary side, to be injected into the power grid, and to charge the BESS, as can be seen on the schematic presented in Figure 1a. In Figure 1b it is possible to identify the different modes of operation allowed by the proposed multifunctional topology.

Figure 2 shows the pulse-width modulation (PWM) sequence pulses and the receivers of the extracted power. It must be clarified that this PWM sequence does not have a fixed duty cycle or a fixed switching frequency and those characteristics are determined by the output variable of the MPPT control algorithm ( $\delta_{MPPT}$ ) or the BESS control algorithm ( $\delta_{BESS}$ ). If there is no need to charge the BESS, the instant imposed by  $\delta_{BESS}$  can be ignored, switching the two metal–oxide–semiconductor field-effect transistor (MOSFET) devices at the same frequency of 100 kHz. Otherwise, the sequence of pulses generated is similar to that shown in Figure 2, showing that the switching frequency of  $S_1$  is twice the one applied on  $S_2$ . Once the  $\delta_{MPPT}$  and  $\delta_{BESS}$  values are obtained, the control system will have to determine the pulse sequence to be applied. For a given switching period, the produced PWM signals are shown in Figure 2, and they range from zero (ZRO) to a period (PRD). Thus, at the ZRO instant, the PWM signals from each of the semiconductors  $S_1$  and  $S_2$  are active. When the value of the modulating wave,  $v_{tri\_PWM}$ , is equal to the comparator A,  $CMPA$ , the semiconductors  $S_1$  and  $S_2$  are open. As soon as  $v_{tri\_PWM}$  reaches a value equal to comparator B,  $CMPB$ , only the MOSFET  $S_1$  is active. In turn, when the value of  $v_{tri\_PWM}$  reaches a value equal to the comparator C,  $CMPC$ , only the MOSFET  $S_2$  is active. This state is maintained until the end of the switching cycle. In the end,  $v_{tri}$  restarts with zero value, at the instant ZRO, initiating a new switching cycle. It should be highlighted that the digital signal controller (DSC) of Texas Instruments has control registers with names equal to the variables used.

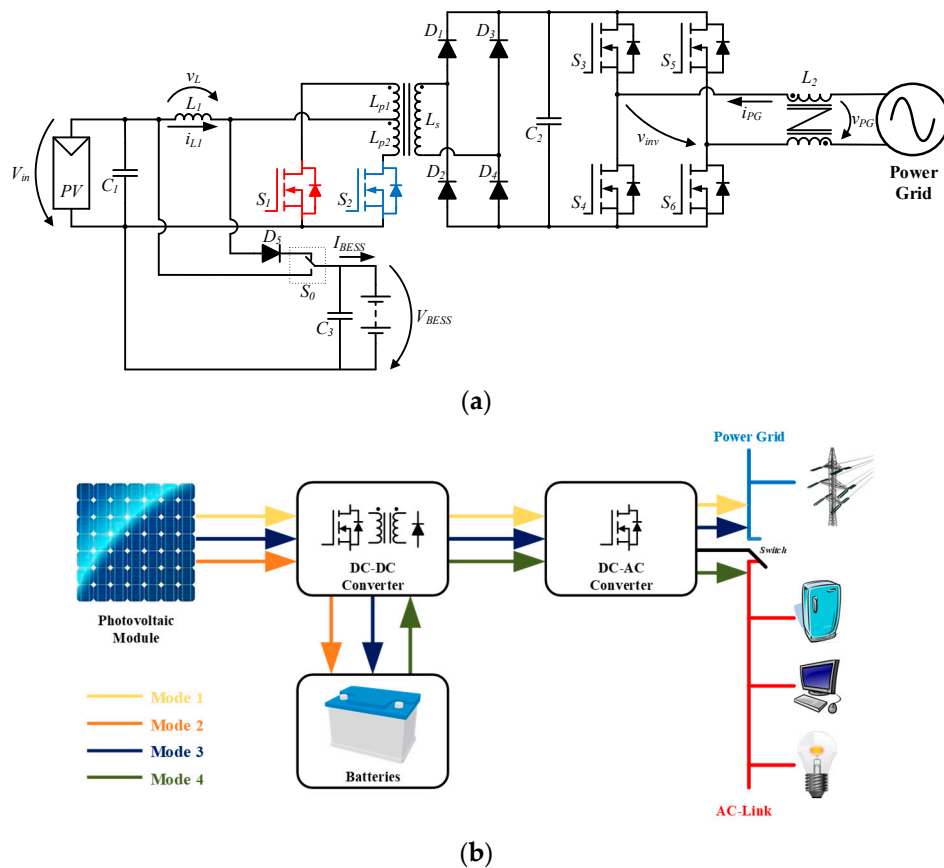


**Figure 1.** Topology and operation modes of the proposed multifunctional isolated microinverter: (a) Schematic of the microinverter topology; (b) Representation of the operation modes.

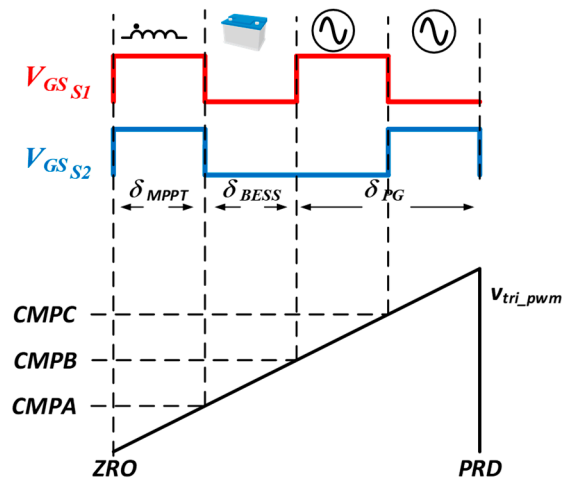


**Figure 2.** Signal sequence to obtain the pulse-width modulation (PWM) signals for the semiconductors  $S_1$  and  $S_2$ .

Regarding the comparison values, they acquire the integer values from the MPPT and BESS control algorithms. That is, the  $CMPA$  variable takes the value of  $\delta_{MPPT}$ , as shown in Equation (1), and the  $CMPB$  variable has a value equal to the sum of the variables of  $\delta_{MPPT}$  and  $\delta_{BESS}$ , as shown in Equation (2). The excess time, which is represented by  $\delta_{PG}$ , is equal to the difference of the switching period,  $PRD$ , with the  $CMPB$ , as shown in Equation (3). The final result is divided by two and added

to the  $CMPB$  value in order to obtain the  $CMPC$  value, as shown in Equation (4), as well as to obtain a symmetry in the waveform.

$$CMPA = \delta_{MPPT} \quad (1)$$

$$CMPB = \delta_{MPPT} + \delta_{BESS} \quad (2)$$

$$\delta_{PG} = PRD - CMPB \quad (3)$$

$$CMPC = CMPB + \frac{\delta_{PG}}{2} \quad (4)$$

### 2.1. System Architecture

The main purpose of the multifunctional isolated microinverter is to inject all the available power from the solar PV module into the point of consumption. If the power extracted from the solar PV module is higher than the consumption, the surplus production can be stored in the BESS during the daylight hours, to be later used in the night period. Considering the surplus energy and the state-of-charge of the BESS, a battery charging current reference is determined. For that reason, additional hardware to measure the loads power consumption is necessary, which is out of the scope of this paper. However, to preserve the state-of-health of the BESS, an optimal charging algorithm is activated periodically, considering the manufacturer's recommendations. The versatility of the proposed topology enables several operation modes presented in Figure 1b which are as follows: mode 1 (PV to PG)—when the consumed power exceeds the power provided by the solar PV modules, all the extracted power is injected into the power grid; mode 2 (PV to BESS)—if there is no consumption in the home (or during power grid outages) and the BESS is not fully charged, then the power from the solar PV module is used to charge the BESS; mode 3 (PV to PG and to BESS)—when the power produced exceeds the consumed power, the surplus is used to charge the BESS; mode 4 (BESS to PG)—during the night or power grid outages, the system detects it and provides the available energy that was previously stored for the point of consumption. Regarding the operation Mode 4, the switch  $S_0$  changes state, allowing the connection of the BESS to the microinverter input, entering a current source operating mode, with the DC–DC power converter responsible for the regulation of the DC-Link and the DC–AC converter responsible for the injection of energy into the local power grid. However, this paper only explores the modes of operation with the solar PV modules, thus showing only the first three modes of operation.

### 2.2. Operation Principle

In order to control the flow of energy, the push–pull power converter MOSFET needs to operate with the switching sequence represented in Figure 1a. In the first state represented in Figure 3a (from  $t_0$ – $t_1$ ), both MOSFET,  $S_1$  and  $S_2$ , are turned-on, making the inductor current,  $i_{L1}$ , flow through the primary transformer windings,  $L_{p1}$  and  $L_{p2}$ . Once the induced magnetic flux has opposite directions, a magnetic short circuit is created. During this time, the inductor voltage,  $v_{L1}$ , is equal to the input voltage,  $v_{in}$ , and  $L_1$  stores energy. Additionally, and once the diode  $D_5$  is inversely polarized, the BESS is charged only with the energy stored in capacitor  $C_3$ . In the second state (between  $t_1$ – $t_2$ )  $S_1$  and  $S_2$  are turned-off, as can be seen in Figure 3b, forcing  $i_{L1}$  to flow to the BESS. During this time, the energy produced by the solar PV module and the energy stored in  $L_1$  are used to charge the BESS and to  $C_3$  through the  $D_5$ . These two states operating in sequence will enable the push–pull power converter to operate as a conventional step-up power converter. The final two states (between  $t_2$ – $t_3$  and between  $t_3$ – $t_4$ ), are responsible for sending energy to the secondary side of the transformer. First, and with only  $S_1$  turned-on as represented in Figure 3c,  $i_{L1}$  passes through  $L_{p1}$ , inducing a voltage on the secondary winding,  $L_s$ . Finally, in Figure 3d, only  $S_2$  is turned-on. This state is similar to the previous one, however this time it is the other primary winding,  $L_{p2}$ , responsible for inducing a voltage in  $L_s$ . It should be emphasized that when  $S_1$  is turned-on, the voltage in  $L_{p1}$  is the double of  $v_{in}$ , (resulting in the sum of  $v_{in}$  with  $v_L$ ). Additionally, due to the magnetic coupling, this voltage is reflected in the

other two windings,  $L_{p2}$  and  $L_s$ , considering the transformer turns ratio. At this instant, the MOSFET  $S_2$  needs to withstand a drain-source voltage four times higher than  $v_{in}$ , resulting in the sum of  $v_{in}$ ,  $v_L$ , and the voltage on  $L_{p2}$ . This is also true for MOSFET  $S_1$ , when  $S_2$  is turned-on and  $S_1$  turned-off.

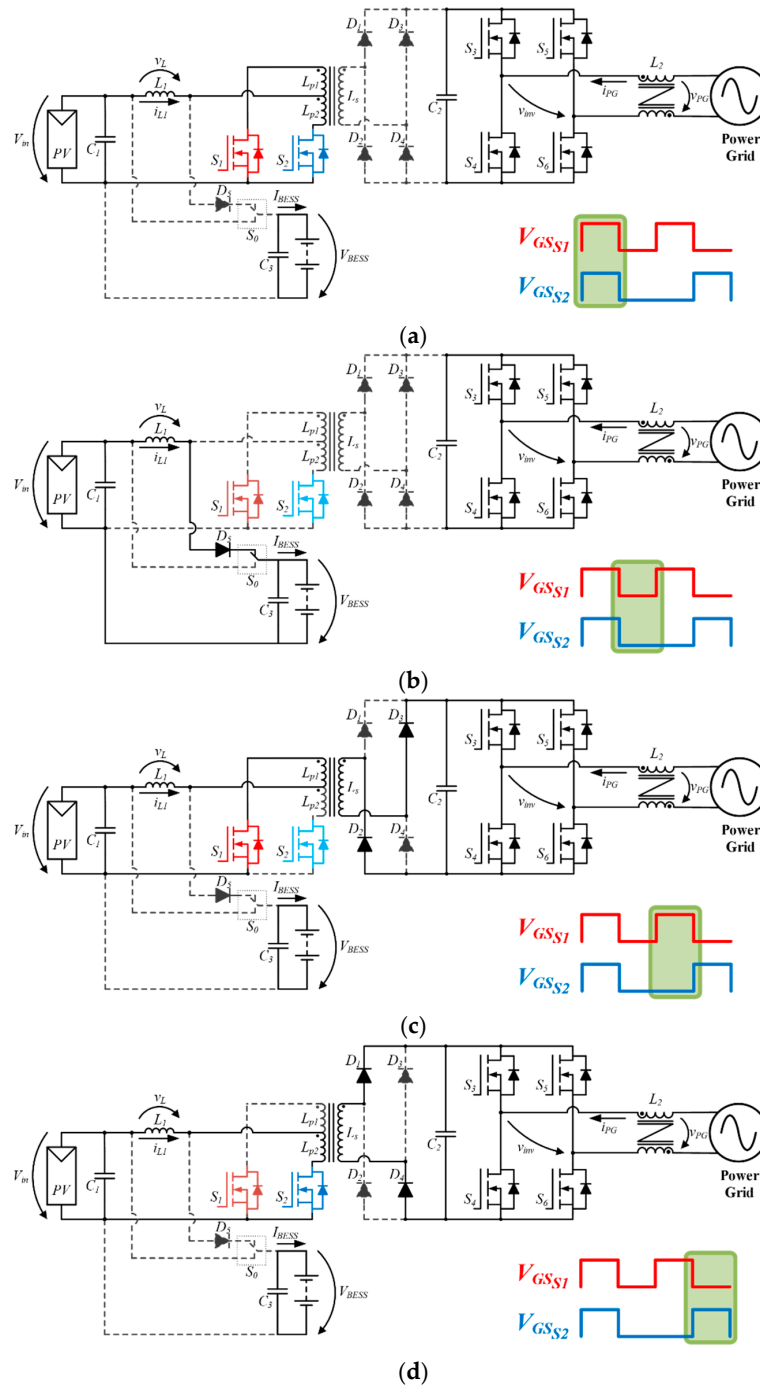


**Figure 3.** Operation states of the microinverter for the first three modes: (a) metal–oxide–semiconductor field-effect transistor (MOSFET)  $S_1$  and  $S_2$  turned-on, creating a magnetic short-circuit into the high frequency transformer; (b) MOSFET  $S_1$  and  $S_2$  turned-off, charging the battery energy storage system (BESS); (c) Only MOSFET  $S_1$  is turned-on, sending energy to the secondary winding of the transformer by  $L_{p1}$ ; (d) Only MOSFET  $S_2$  is turned-on, sending energy to the secondary winding of the transformer by  $L_{p2}$ .

### 3. Control Algorithms

The proposed control structure comprises the MPPT, the BESS charging, the DC-link voltage control and the current control algorithms. The controllers were adjusted in order to guarantee a continuous and correct operation of the multifunctional isolated microinverter.

#### 3.1. MPPT Control Algorithm

The solar PV modules, ideally, should always operate at the MPP. However, the temperature and the radiation directly influence the power produced by the solar PV cells. These external factors are responsible for the current and voltage variations in each solar PV module, and consequently, on the total power available [22]. For this reason, an MPPT control algorithm is used in order to find the MPP and continuously impose the DC–DC power converter operation at this point. In the literature, there are different MPPT algorithms, with diverse complexities and effectiveness [22–24]. Constant current, constant voltage, perturbation and observation, and incremental conductance are some examples of MPPT control algorithms.

The incremental conductance MPPT control algorithm is based on the characteristic curve of the solar PV module to find the MPP. In fact, when the system is operating at the MPP, the derivative of the module's output power in relation to the voltage is zero. By deriving the PV power in relation to voltage, Equation (5) is obtained.

$$\frac{dP}{dV} = \frac{d(VI)}{dV} = V \frac{dI}{dV} + I = I + V \frac{\Delta I}{\Delta V} \quad (5)$$

By equalizing the power derivative in relation to the voltage at zero, the MPP can be found by comparing the instantaneous conductance with the incremental conductance, as shown in Equation (6).

$$\frac{dP}{dV} = 0 \Leftrightarrow I + V \frac{\Delta I}{\Delta V} = 0 \Leftrightarrow \frac{\Delta I}{\Delta V} = -\frac{I}{V} \quad (6)$$

In turn, when the derivative is positive, the system is operating at the left of the MPP. When the derivative is negative, the system operates on the right side of the MPP. This conclusion is summarized in Table 1.

**Table 1.** Summary of the power behavior with the incremental conductance maximum power point tracker (MPPT) control algorithm.

Condition	Working Point	Next Operation
$\frac{dP}{dV} = 0$	On the MPP	Keep the control variable
$\frac{dP}{dV} > 0 \Leftrightarrow \frac{\Delta I}{\Delta V} > -\frac{I}{V}$	In the left of the MPP	Increase the control variable
$\frac{dP}{dV} < 0 \Leftrightarrow \frac{\Delta I}{\Delta V} < -\frac{I}{V}$	In the right of the MPP	Decrease the control variable

For practical implementation, the voltage and the current values are acquired in the solar PV modules in order to be able to calculate the variation of the respective values with the previous iteration. The main condition to be verified is whether the system is at the MPP, represented by Equation (6). If this is the case, only the voltage and current values are updated. Otherwise, it is necessary to check whether the system is on the left or on the right of the MPP in order to be able to carry out the appropriate correction to converge to the MPP. The increment step will determine how quickly the converter operates on the MPP. However, if the increment is too high, the system will be oscillating around the MPP [23]. The flowchart of the incremental conductance control algorithm is presented in Figure 4a, and an example of the MPPT control algorithm implemented in C language is exposed in Figure 4b.

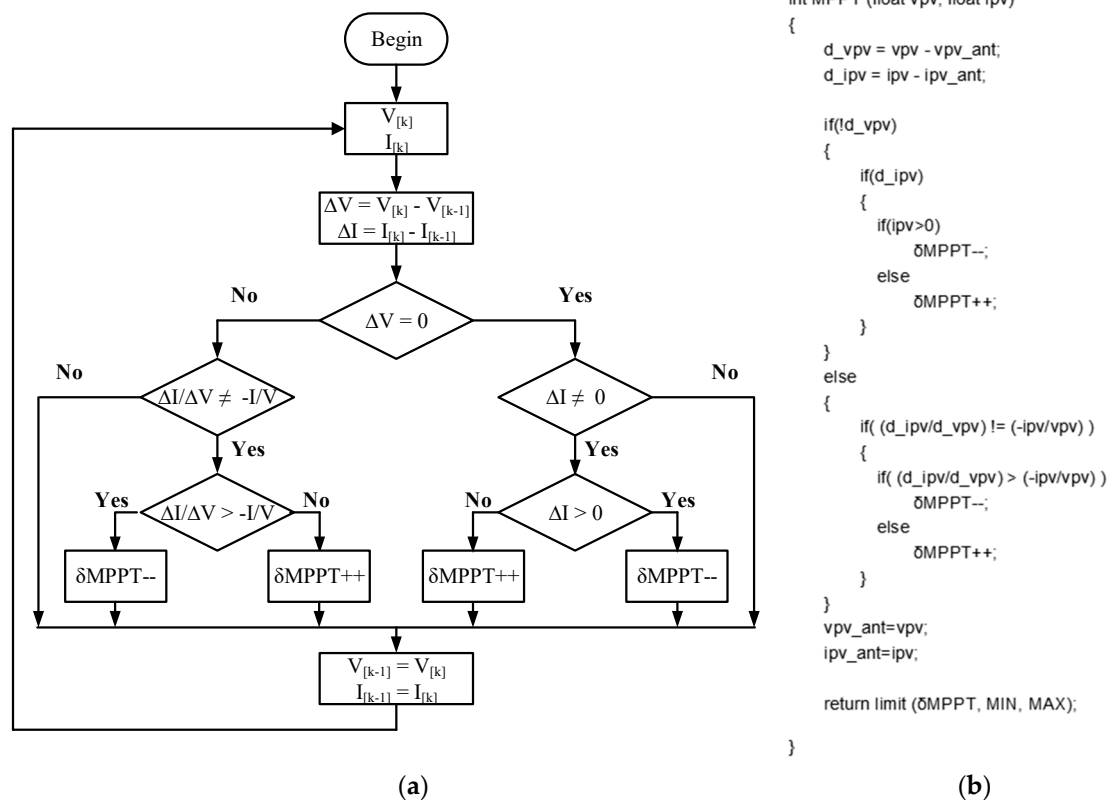


**Figure 4.** Incremental conductance maximum power point tracker (MPPT) control algorithm: (a) Flowchart of the control algorithm; (b) Example of the control algorithm implemented in C language.

After this revision, the incremental conductance MPPT control algorithm was chosen to be implemented, since it presents interesting features for a solar PV installation despite its complexity of implementation. It should be noted that a low frequency—a few hundred Hertz—of operation of the MPPT algorithm was chosen since solar radiation and temperature, the main factors that influence power, are practically constant over short periods of time of milliseconds. In this way, it is possible to mitigate any measurement noise from the system, using for this purpose a sliding average of the measured values.

### 3.2. BESS Charging Control Algorithm

Considering that this topology interfaces a sensitive system such as the BESS, where the manufacturer recommended some specific operating conditions in order to preserve the battery's lifetime, a specific BESS charging control algorithm was implemented. There is extensive information on control algorithms for this purpose. In [25], some of the existing algorithms are presented. Figure 5 presents the constant current followed by constant voltage control adopted for the implementation of the BESS charging control algorithm. This control algorithm consists of two charging stages. In the first stage, a constant current is applied until the battery reaches its nominal voltage, then, the second stage is activated, by applying a constant voltage to the battery terminals until the charging current reaches residual values. The typical behavior of the battery voltage and current waveforms of this algorithm is shown in Figure 5.

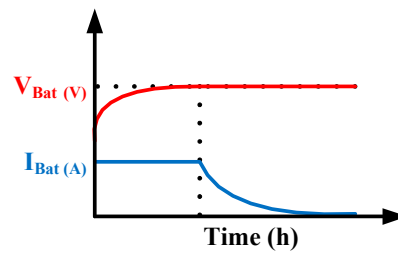


**Figure 5.** Representation of the two stages of the constant current followed by the constant voltage control algorithm.

This control algorithm is normally used in lithium-ion and lead–acid batteries. Sometimes, in lead–acid batteries, a third charging stage is added, maintaining the applied voltage for an indefinite time. This stage is called a float charge [25]. However, in all the charging algorithms mentioned above, the values of charging voltages and currents vary with the configuration and technology of the cells that constitute the battery. Thus, it is necessary to consult the information provided in the manufacturers’ datasheets.

Considering the present application in which lead-acid batteries were used, for validation purposes, it was selected the constant-current followed by the constant-voltage charging algorithm.

### 3.3. DC-Link Voltage Control Algorithm

The conventional microinverter has the main purpose of injecting the DC power resulting from the solar PV module into the power grid. In this framework, the DC-link voltage of the DC–AC power convert must be higher than the peak of the power grid voltage, since the DC–AC power converter is a voltage source inverter. Once the DC–DC power converter is responsible for extracting the maximum power from the solar PV module, the DC–AC power converter has to regulate the DC-link voltage in order to maintain continuous operation. The calculations of the reference current,  $i^*$ , are presented in the block diagram of Figure 6b. For this reason, the control system continuously monitors all variables that can influence the DC-link voltage, such as the average input power from the solar PV module,  $\overline{P}_{in}$ , the average power used to charge the BESS,  $\overline{P}_{BESS}$ , the average DC-link voltage,  $\overline{V}_{DC}$ , and the voltage in the power grid,  $v_{PG}$ . The control system determines the error,  $V_{DC\_error}$ , between the DC-link reference voltage,  $V_{DC^*}$ , and the average value of the voltage in the DC-link,  $v_{DC}$ . The resulting error,  $V_{DC\_error}$ , is fed to a proportional–integral (PI) controller, which is responsible for calculating the required power,  $P_{REG}$ , in order to maintain the DC-link voltage regulated. The difference between  $P_{in}$  with  $P_{REG}$  and  $P_{BESS}$  is divided by the square of the root mean square (RMS) voltage value of the power grid,  $V_{pll}$ , resulting in the conductance,  $G$ , as shown in Equation (7). Simultaneously, the phase-locked loop (PLL) control algorithm represented in Figure 6a is responsible for generating a unitary sinusoidal waveform,  $v_{pll}$ , with a frequency and phase equal to the fundamental component of the power grid voltage (50 Hz), and its peak voltage value,  $\hat{V}_{pll}$ , [26,27].

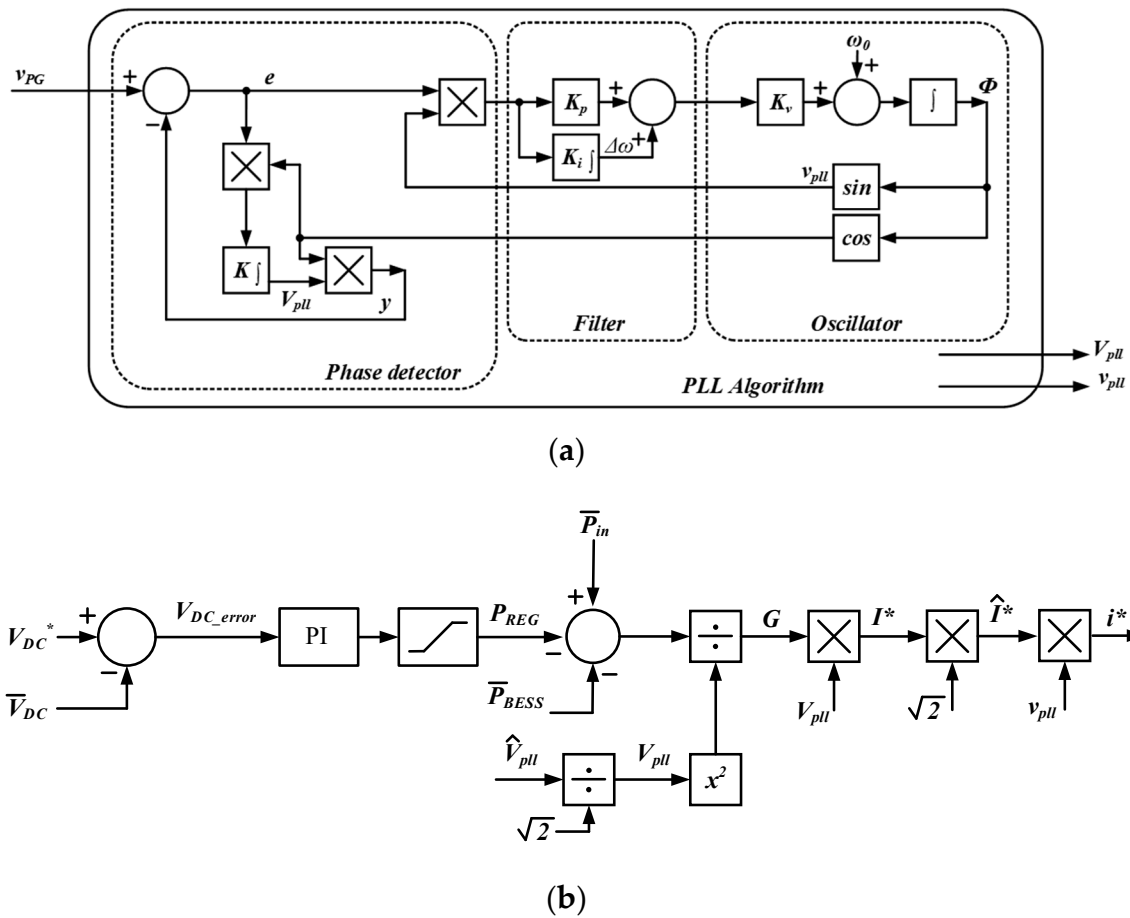


**Figure 6.** Block diagrams of the multifunctional isolated microinverter controls: (a) Phase-locked loop (PLL) control algorithm block diagram; (b) Current reference calculation block diagram.

The reference current,  $i^*$ , which the DC–AC power converter has to synthesize, results from the multiplication of  $G$  with  $v_{pll}$ ,  $V_{pll}$  and  $\sqrt{2}$ , as in Equation (8).

$$G = \frac{\bar{P}_{in} - \bar{P}_{Bat} - P_{REG}}{(V_{pll})^2} \tag{7}$$

$$i^* = \sqrt{2} G V_{pll} v_{pll} \tag{8}$$

### 3.4. Current Control Algorithm

Once the reference signal,  $i^*$ , is established, the DC–AC power converters need a control algorithm to produce an output current,  $i_{PG}$ , equal to  $i^*$ . This algorithm takes advantage of a feedback loop in order to calculate the voltage value to be generated by the power converter,  $v_{inv}^*$ , obtaining the desired current. For this kind of application, with a full bridge DC–AC power converter, there are several current control algorithms [26,28–30]. A very interesting option is the predictive control [26,30], where this control algorithm uses the electrical model of the system to predict the future behavior of the control variable. Observing the DC–AC power converter depicted in Figure 1a, it can be identified that the inverter voltage,  $v_{inv}$ , is equal to the sum of the voltage across the coupling inductance,  $v_{L2}$ , with the power grid voltage,  $v_{PG}$ , as shown in Equation (9). Considering the inductance characteristic equation, and the current error,  $i_{error}$  (resulting from the difference between  $i^*$  and  $i_{PG}$ ), it is possible to obtain Equation (10). If Equation (10) is passed to the discrete domain, Equation (11) is obtained. For a small sampling period,  $T_s$ , it can be considered that the variation of  $i_{error}$ , is almost constant.

Additionally, it can be concluded that the effectiveness of this control technique is directly influenced by the quality of the considered system model [31].

$$v_{inv} = v_{L2} + v_{PG} \quad (9)$$

$$v_{inv} = L \left( \frac{di^*}{dt} - \frac{di_{error}}{dt} \right) + v_{PG} \quad (10)$$

$$v_{inv}^*[k] = v_{PG}[k] + \frac{L}{T_S} (2i^*[k] - i^*[k] - i_{PG}[k]) \quad (11)$$

### 3.5. Control System

Figure 7 shows the block diagram of the microinverter, highlighting the measured and the control variables, as well as the control system algorithms. By analyzing this figure, the sequence of operations is evident, including acquisition of control signals, processing of acquired values, and driving of semiconductor switching devices.

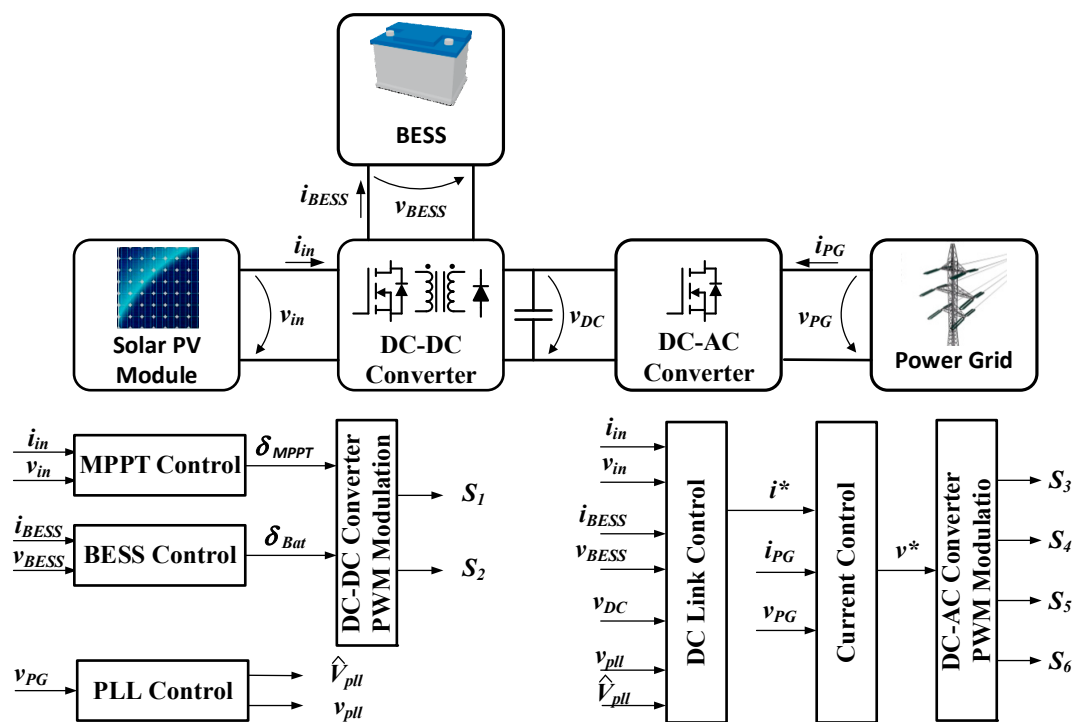


Figure 7. Block diagram of the microinverter with the integration of the control algorithms.

By analyzing Figure 7, it is possible to perceive the existence of two input control algorithm blocks: MPPT Control and BESS Control. The MPPT control algorithm is the responsible for the extraction of the maximum power from the solar PV module, with the  $\delta_{MPPT}$  being the output control variable. On the other hand, the BESS charging control algorithm generates the  $\delta_{BESS}$  output control variable. These output variables are later used to generate the gate pulses of the MOSFET switching devices  $S_1$  and  $S_2$  that contribute to the operation of the high-frequency DC–DC power converter.

The PLL control algorithm is responsible for the acquisition of the phase-angle and amplitude of the fundamental component of the power grid voltage. The signals resulting from this block are subsequently used to synchronize the microinverter with the power grid.

Finally, it is possible to verify the existence of three sequential blocks, responsible for regulating the DC-link voltage, generating the reference current, and controlling the DC–AC power converter. The first block, named DC-link control, consists in the acquisition of the different system variables

necessary for the synthesis of a reference current,  $i^*$ , and is responsible for the regulation of the DC-link voltage. Then, the  $i^*$  signal, together with the signals from the PLL algorithm, enter the block of current control responsible for generating the reference voltage,  $v^*$ , that, when compared to the triangular carrier, generates the activation signals for the MOSFETs  $S_3$  to  $S_6$  that operate the DC–AC power converter.

#### 4. Simulation Results

In this section, some simulation results of the proposed topology are presented and discussed, as well as a detailed description of the three of the four allowed operation modes. In order to achieve accurate results, some implementation aspects, such as a model of solar PV module for the Kyocera KC200GHT with a maximum power of 200 W<sub>p</sub>, as well as a battery equivalent model, were employed for the simulation model. It was considered that the solar PV module operated under standard test conditions, which are 1000 W/m<sup>2</sup> and 25 °C. Regarding the BESS, the Thevenin equivalent model represented in Figure 8 was considered. The Thevenin equivalent model uses an ideal voltage source ( $E_0$ ), representing the BESS nominal voltage, and an equivalent series resistor ( $ESR$ ) in series with the capacitor  $C_{Bat}$  parallel to the resistor  $R_{Bat}$ . The  $ESR$  represents the internal resistance of the battery, and the  $C_{Bat}$  with the  $R_{Bat}$  are used to predict the battery response for a load transient. Despite the minimalistic concept of the present model, considering only constant values in the parameters during the simulation and, consequently, a constant state-of-charge, it manages to replicate with some accuracy the variation of voltage,  $V_{Bat}$ , during charging and discharging processes. Consequently, the Thevenin equivalent model was adopted to validate the proposed topology. Additional dynamic models for the batteries are presented in [32].

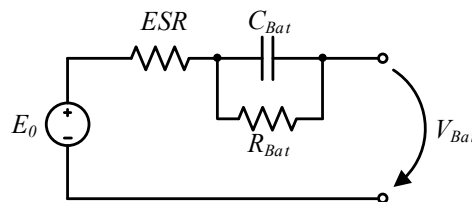


**Figure 8.** Equivalent Thevenin electrical model for the battery energy storage system (BESS).

In order to meet the real operating conditions, the BESS was designed for a storage capacity of 500 Wh. Since the DC–DC power converter behaves as a step-up power converter, the BESS has to be designed for a minimum voltage higher than the maximum voltage of the solar PV module, so a nominal voltage of 36 V was adopted, corresponding to three 12 V lead-acid batteries connected in series. To preserve the batteries, a maximum discharge depth,  $p$ , of 25% was defined, according to battery manufacturer recommendations. Based on Equation (12), the capacity of the BESS was dimensioned.

$$\text{Capacity} = \frac{\text{Storage Capacity (Wh)}}{V_{Bat}(\text{V}) p(\%)} = \frac{500}{3 \times 12 \times 0.25} = 55.6 \text{ Ah} \quad (12)$$

According to the obtained results, three commercial 12 V-55 Ah lead-acid batteries were selected. Thus, for a battery with a capacity of 55 Ah and with the aid of Equation (13), the value for the capacitor of the Thevenin equivalent model represented in Figure 8,  $C_{Bat}$ , is obtained through Equation (14).

$$C_{Bat} = \frac{Q}{V} \quad (13)$$

$$C_{Bat} = \frac{55 \times 3600}{36} = 5500 \text{ F} \quad (14)$$

However, using this value in the simulation model would require a very long simulation time to proceed with a 25% deep discharge–charging cycles. In order to simplify the model and proceed

with a faster simulation, a ratio of 1:3000 was considered, thus considering a capacity of 1.8 F. Thus, considering a battery simulation charging time of 3.5 s, as shown in Figure 9, it is equivalent to a charging time of approximately 3 h in an experimental application.

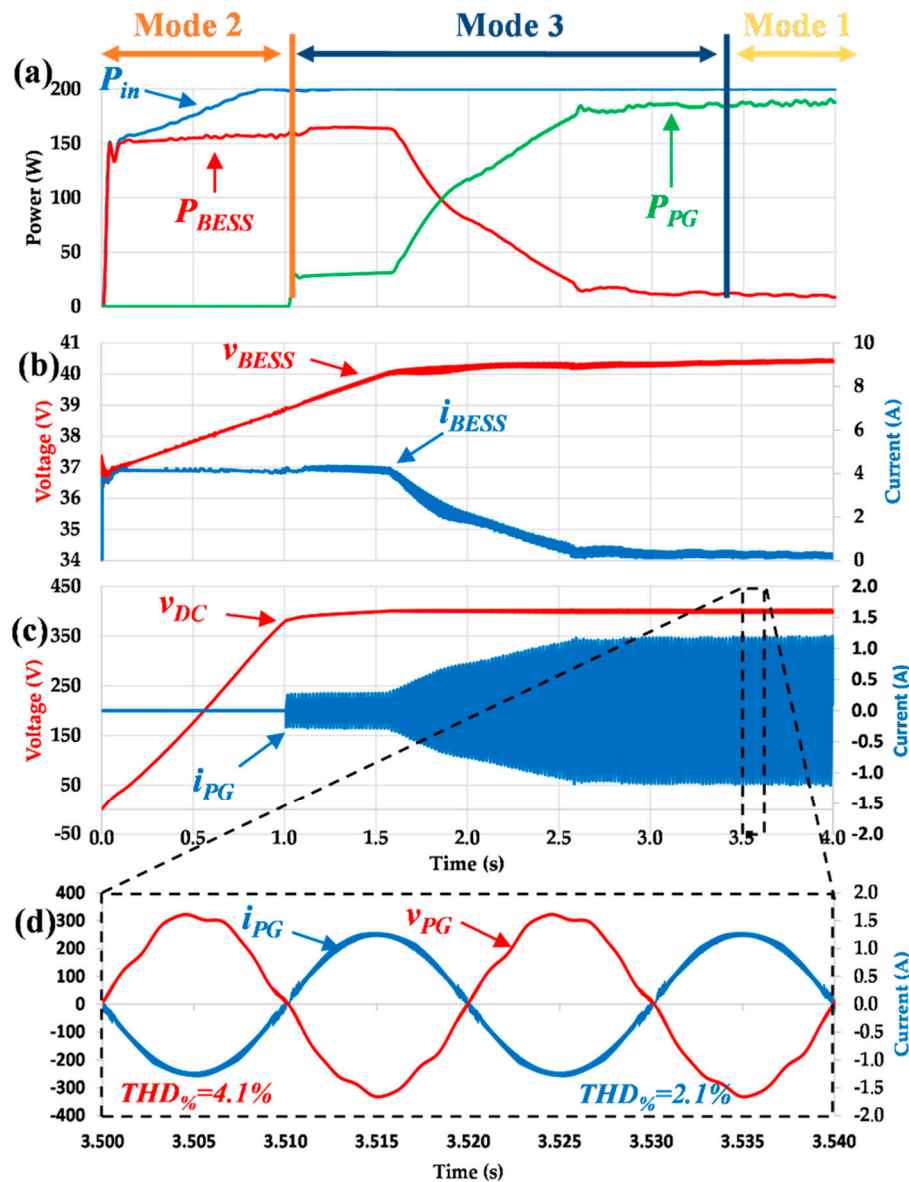


**Figure 9.** Simulation results of the multifunctional isolated microinverter: (a) Input power ( $P_{in}$ ), power used to charge the BESS ( $P_{BESS}$ ) and power injected into the power grid ( $P_{PG}$ ); (b) Voltage ( $v_{BESS}$ ) and current ( $i_{BESS}$ ) during the BESS charge; (c) DC-link regulation, showing the voltage in the DC-link ( $v_{DC}$ ) and the current ( $i_{PG}$ ) produced by the DC-AC power converter; (d) Detail of the current ( $i_{PG}$ ) and voltage ( $v_{PG}$ ) of the power grid.

Table 2 presents the values of the main components used to simulate the high-frequency multifunctional microinverter. The values of the components used were obtained from a preliminary theoretical estimation based on [26] and then optimized according to the simulation results as well as after considering the material available in the laboratory. A design procedure for an LCL filter is presented in [33]. In order to approximate the simulation model to reality, the used power grid voltage is not sinusoidal, but similar to the voltage at the power electronics laboratory where the experiments were performed. For this purpose, a Fluke-435 power quality analyzer was used to measure and

register the harmonic spectrum of the phase voltage at the laboratory facility. The obtained values are shown in Table 3.

**Table 2.** Specification of the simulation parameters.

Description	Variables	Value	Units
Input inductance	$L_1$	330	$\mu\text{H}$
Output inductance	$L_2$	8	mH
Input capacitance	$C_1$	470	$\mu\text{F}$
DC-link capacitance	$C_2$	470	$\mu\text{F}$
BESS capacitance	$C_3$	470	$\mu\text{F}$
Line inductance	$L_z$	200	$\mu\text{H}$
Line resistance	$R_z$	0.1	$\Omega$
BESS Thevenin model internal resistance	$ESR$	0.1	$\Omega$
BESS Thevenin model internal capacitance	$C_{Bat}$	1.8	F
BESS Thevenin model nominal voltage	$E_0$	36	V
DC-link nominal voltage	$v_{DC}$	400	V
High-frequency transformer turns ratio	-	1:1:10	
Push-pull MOSFET switching frequency	-	100/200	kHz
DC-AC MOSFET switching frequency	-	50	kHz
Sampling frequency	-	50	kHz

**Table 3.** Harmonic spectrum of the power grid voltage measured at the power electronics laboratory used in the simulation models.

Harmonic Order	$V_{\text{RMS}}$ (V)	Phase-Angle ( $^\circ$ )
1	228	0
3	1	95
5	0.6	135
7	8.3	44
9	1.6	-147
11	3.7	-134
13	0.2	29
15	0.3	-20
THD%	4.13%	

Figure 9 combines the simulation results of the multifunctional isolated microinverter performing the BESS charging with constant current followed by constant voltage, and injecting the remaining energy from PVs in the PG. At the instant  $t = 0$  s, represented in Figure 9a, the MPPT and the BESS control algorithms are enabled, starting to extract the maximum power available from the solar PV module to charge the BESS with a constant current. Some energy was used to charge the DC-link, with the DC-AC power converter being disabled until the voltage in the DC-link reaches the stipulated value (mode 2). Once the DC-link reaches the stipulated voltage, the DC-AC starts to inject energy into the PG, maintaining the DC-link voltage-regulated in the reference value (mode 3). Once the BESS is fully charged, all available PV power is injected in the PG (mode 1). In this operation mode, it can be verified that the multifunctional isolated microinverter gets the MPP and continuously operates at this point. Figure 9b shows the BESS charging algorithm, consisting of a constant current followed by constant voltage. In Figure 9c, it is possible to see the beginning of operation of the DC-AC power converter, adjusting the  $i_{PG}$  amplitude in order to maintain the DC-link voltage regulated. Figure 9d shows a detail of the power grid current,  $i_{PG}$ , with a phase shift of  $180^\circ$  related to the fundamental component of the power grid voltage,  $v_{PG}$ .

In Figure 10, it is possible to see in more detail, and at different time periods of operation of the multifunctional isolated microinverter, the influence of the  $\delta_{MPPT}$  and  $\delta_{BESS}$  control variables from the MPPT and BESS control algorithms. In general, it is possible to verify that the value of  $\delta_{MPPT}$  imposes the time that the semiconductors  $S_1$  and  $S_2$  are simultaneously in conduction (the current in

the inductor  $L_1$ ,  $i_{L1}$ , rises). The  $\delta_{BESS}$  value controls the time period that the semiconductors  $S_1$  and  $S_2$  are simultaneously open (the energy of the solar PV module and the energy stored in the  $L_1$  inductor in the previous instant flows to the BESS, as a consequence, the BESS current increases). The remaining time of the control period is divided into two equal time intervals, with only one of the semiconductors ( $S_1$  or  $S_2$ ) conducting at each of these time intervals (the energy is directed to the secondary side of the high-frequency transformer, thus reflecting a voltage on the secondary side proportional to the voltage existing at the primary winding terminals of the high-frequency transformer).

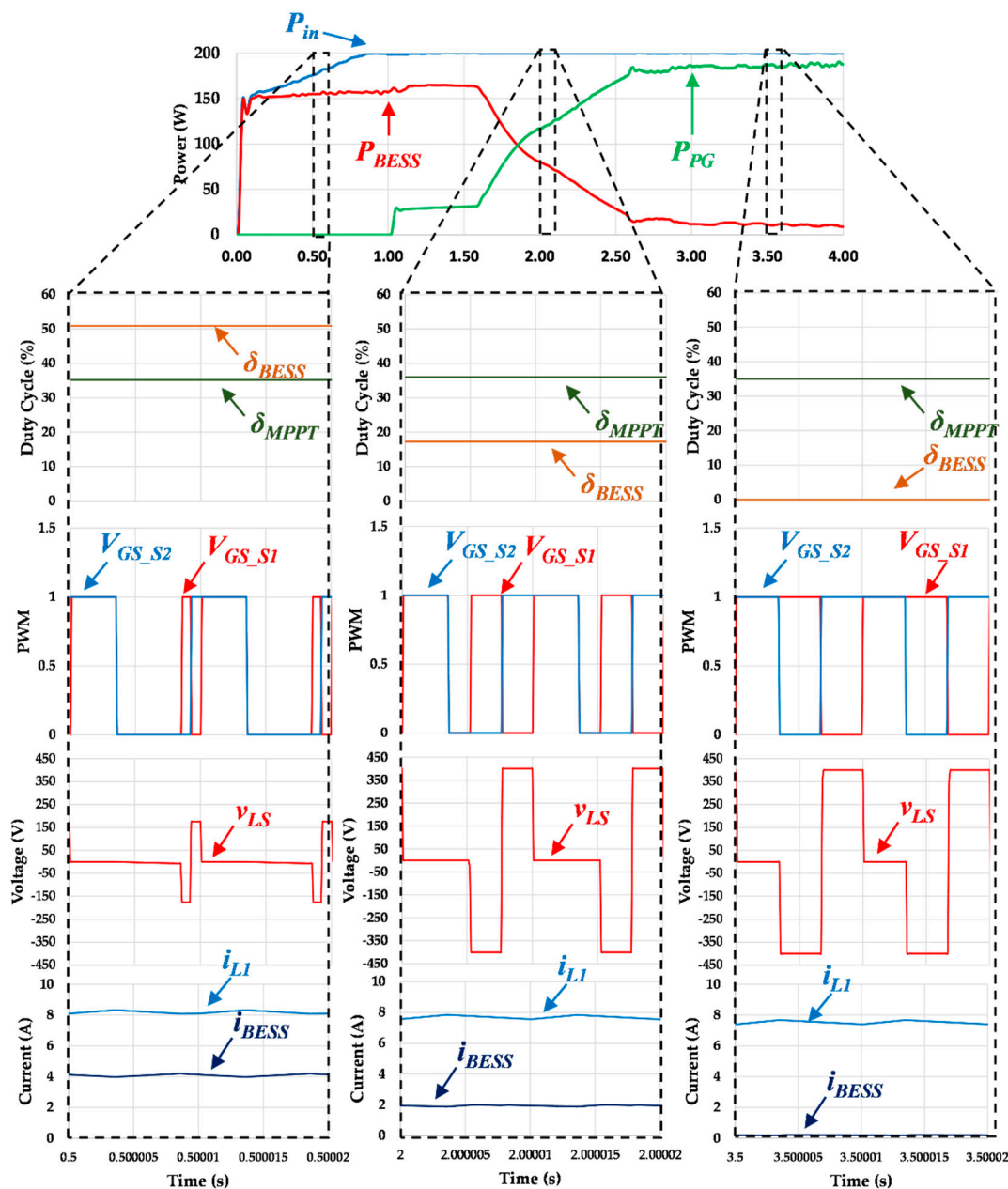


**Figure 10.** Identifiable influence of the  $\delta_{MPPT}$  and  $\delta_{BESS}$  control variables from the MPPT and BESS charging control algorithms at different time intervals:  $V_{GS\_S1}$ —MOSFET  $S_1$  gate–source PWM signal;  $V_{GS\_S2}$ —MOSFET  $S_2$  gate–source PWM signal;  $v_{LS}$ —voltage at the secondary winding terminals of the high-frequency transformer;  $i_{L1}$ —input current measured on inductor  $L_1$ ;  $i_{BESS}$ —BESS charging current.

In order to determine the efficiency of the proposed multifunctional microinverter, the input power and output power of the microinverter were analyzed in the most important operating modes:

operation mode 1, when the microinverter uses all the energy coming from the photovoltaic solar module to inject into the PG, and operation mode 3, when the microinverter uses energy from the PV solar module to inject into the PG and to charge the battery. The results obtained are shown in Figure 11a,b, in which the different efficiencies of the system for different values of radiation and operating temperature are noted.

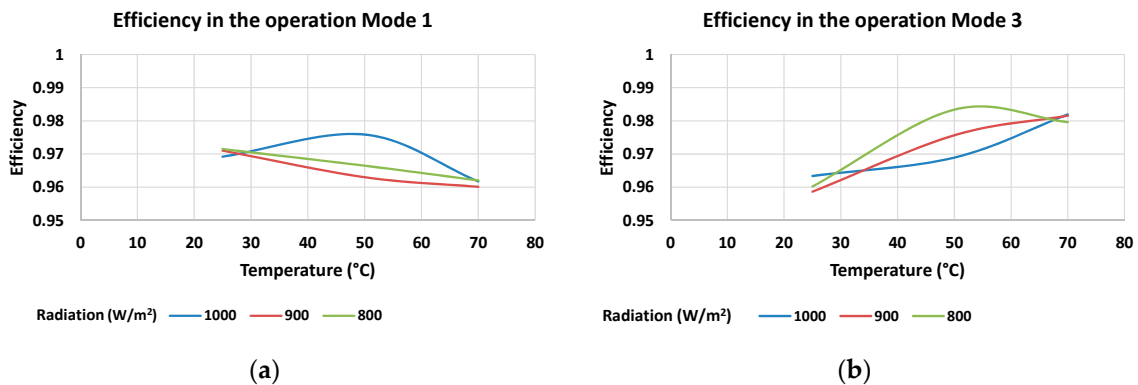


**Figure 11.** Multifunctional microinverter efficiency during: (a) Operation mode 1; (b) Operation mode 3.

## 5. Multifunctional Isolated Microinverter Prototype

The main objective of this research work is to develop and validate a new multifunctional isolated microinverter topology for solar PV applications. In this way, and in this initial stage of development, instead of using a compact version, a modular implementation was chosen, consisting of individual boards with specific functions such as the signal conditioning board, the control board, the gate driver boards, and the power converters boards. Figure 12 shows a general overview of the laboratory workbench, where the prototype was assembled and tested.

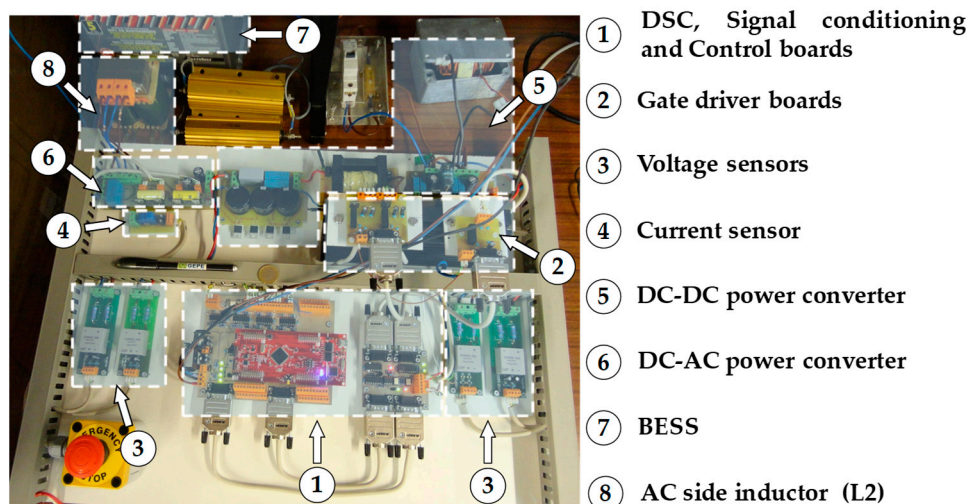


**Figure 12.** Top view of the developed multifunctional isolated microinverter prototype.

### 5.1. Hardware Development

The operation characteristics of the multifunctional isolated microinverter implemented are present in Table 4. In Table 5, the main components used in the laboratory prototype are presented, some of which were developed by the author for the multifunctional isolated microinverter.

**Table 4.** Specification of multifunctional isolated microinverter operating conditions.

Description	Variables	Minimum	Nominal	Maximum	Units
PV input voltage	$v_{in}$	20	26.3	32.9	V
PV input current	$i_{in}$	-	7.61	8.21	A
Batteries voltage	$v_{BESS}$	35	36	40.2	V
Batteries current	$i_{BESS}$	-	4	8.21	A
Switching frequency (DC–DC Converter)	-	100	-	200	kHz
DC-link voltage	$v_{DC}$	370	400	450	V
AC output voltage	$v_{PG}$	207	230	253	V
Switching frequency (DC–AC converter)	-	-	50	-	kHz
Sampling frequency	-	-	50	-	kHz

**Table 5.** List of the main components used in the multifunctional isolated microinverter prototype.

Description	Variables	Reference	Value	Units
DC–DC MOSFETs	$S_1, S_2$	IPP530N15N3	-	-
DC–AC MOSFETs	$S_3-S_6$	IPP50R190CE	-	-
Rectifier diodes	$D_1-D_5$	BYC8-600	-	-
Snubber diodes	$D_{snubber}$	FEP16DT	-	-
Zener diode	$Z_1, Z_2$	BZX85C16	-	-
MOSFET gate resistor	$R_G$	-	6	$\Omega$
Input capacitors (Electrolytic in parallel with polypropylene)	$C_1$	Electrolytic polypropylene	470 330	$\mu\text{F}$ nF
DC-link capacitors (Electrolytic in parallel with polypropylene)	$C_2$	Electrolytic polypropylene	470 100	$\mu\text{F}$ nF
BESS capacitors (Electrolytic in parallel with polypropylene)	$C_3$	Electrolytic polypropylene	470 330	$\mu\text{F}$ nF
Input inductance	$L_1$	-	3	mH
Output inductance	$L_2$	-	6.32	mH
High-frequency transformer	-	-	1:1:10	-

For the control system, it should be mentioned that the Texas Instruments TMS320F28377S DSC included in the LAUNCHXL-F28377S development board was used. This DSC has a 32-bit central processing unit with a 200 MHz clock when the random-access memory (RAM) and a control law accelerator (CLA) are used. The development board allows the interface with different peripherals such as analog-to-digital converter (ADC) channels, PWM channels, digital-to-analog converter (DAC) channels, channels for communication, among others. However, for the generation of PWM signals, the present DSC only has two intermediate comparison records, the CMPA and CMPB. In order to create the CMPC as presented in Figure 2, it would be necessary to implement an interruption to update the comparison values during the switching period, which would decrease the performance of the system. In order to mitigate this problem, three DSC PWM channels were used (EPWM7A, EPWM8A, EPWM8B), one of them, the EPWM7A, common in the two output signals ( $V_{GSS1}$  and  $V_{GSS2}$ ). In this way, the EPWM7A signal is dedicated to generating the signal on the time of operation of the  $\delta_{MPPT}$  variable, making the signal SET at instant zero, ZRO, and CLEAR when the EPWM7A counter value reaches a value equal to  $\delta_{MPPT}$ . In turn, the EPWM8A and EPWM8B signals would be responsible for activating the gate signals of  $S_1$  and  $S_2$ , respectively, during the instant imposed by the  $\delta_{PG}$ . That is, when the triangular reached a value equal to the value of  $\delta_{MPPT}$  plus  $\delta_{BESS}$ , which is compared with the CMPA record of EPWM8, the DSC would make a SET to the signal of EPWM8A. In turn, when the triangular reached a value equal to the sum of  $\delta_{MPPT}$  with  $\delta_{BESS}$  and half the value of  $\delta_{PG}$ , which is compared with the CMPB record of EPWM8 channel, the DSC would make a SET to the EPWM8B signal and a CLEAR to the EPWM8A. Finally, when the counter value reached the maximum value, it is restarted, and the EPWM8A and EPWM8B signals are cleared. For the implementation

of this circuit, two logic OR gates from the SN74HCT32N integrated circuit were used. The circuit implemented to generate the two PWM signals in order to control the MOSFETs  $S_1$  and  $S_2$  is shown in Figure 13.

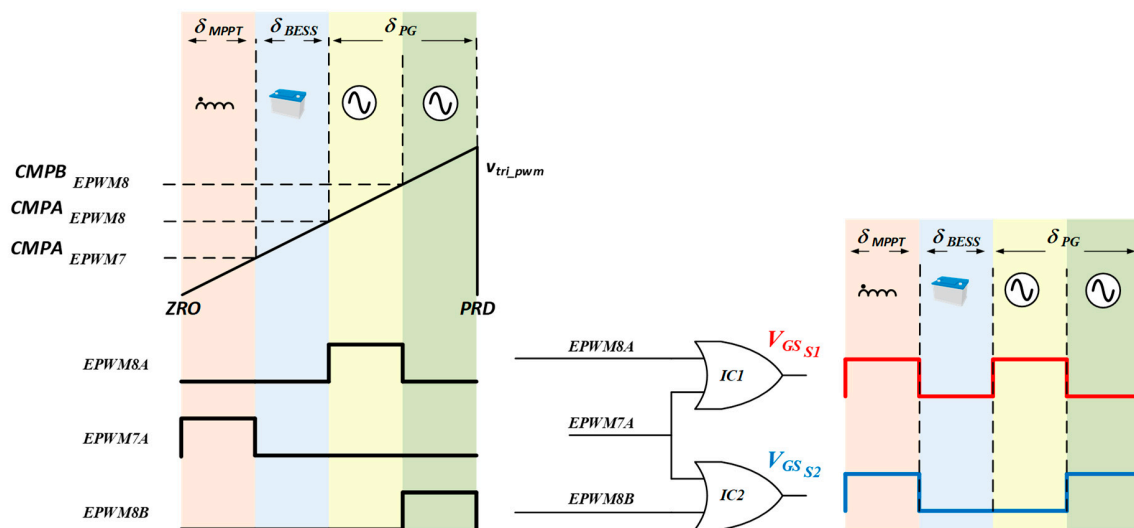


**Figure 13.** Circuit used to obtain the PWM signals for the semiconductors  $S_1$  and  $S_2$ .

### 5.2. Current-Fed Push–Pull DC–DC Power Converter

The hardware of the multifunctional isolated microinverter is composed of the DC–DC followed by the DC–AC power converters. The DC–DC power converter is composed of the input inductor,  $L_1$ , input capacitor,  $C_1$ , two switching devices,  $S_1$  and  $S_2$ , and the high-frequency transformer followed by the high-frequency rectifier.

As previously mentioned, the fully controlled power semiconductors, which constitute the push–pull converter, need to withstand at least the quadruple of the input voltage,  $v_{in}$ . In that regard and for this application, two Infineon IPP530N15N3 MOSFET were used. These withstand a maximum voltage of 150 V and a maximum drain current of 21 A. In addition, they have a low conduction resistance ( $R_{DS\_ON} = 53 \text{ m}\Omega$ ), and propagation times estimated by a few of nanoseconds, allowing for a high switching frequency to be obtained with lower losses. For each MOSFET, a snubber circuit that consists of a  $R_{Sn1}$  resistor, a  $D_{Sn1}$  diode and a  $C_{Sn1}$  capacitor is implemented. The use of fast recovery diodes for the snubber application is recommended. Therefore, diodes with a recovery time of less than 35 ns from the manufacturer VISHAY, model FEP16DT, are used.

The capacitors integrating the microinverter are of two different technologies: electrolytic and polypropylene. The electrolytic capacitor has a higher capacity, while the polypropylene capacitor has a faster response to  $dv/dt$  variations. Accordingly, it was decided to use these two types of capacitors, benefiting from the advantageous characteristics of each type of capacitor.

### 5.3. High-Frequency Transformer

The core of the multifunctional isolated microinverter is the DC–DC power converter where the high-frequency transformer is essential for the correct operation of the system. The high-frequency power transformer should be able not only to transmit energy from the solar PV module to the secondary side, but also to deliver energy, in hours without PV production, from the BESS to the secondary side. For this reason, it was considered a maximum power of 330 W for the high-frequency power transformer. For the correct dimensioning of the high-frequency transformer, the energy losses were considered, being able to identify copper losses and core losses, as shown in Figure 14. It should be noted that the optimal design point does not coincide with the intersection of the copper loss curve with the core loss curve, but where the total power losses are lower. In other words, it is

necessary to relinquish losses of one of the factors in order to maximize the performance of the system. Copper losses are essentially influenced by the conductive material used in the transformer windings, which intrinsically has a given section and a certain length, which will determine the resistance of the winding. In addition, the effective value of the current flowing through the windings will also influence the copper loss. On the other hand, the type of material that constitutes the magnetic core, the flux density and the induced frequency will determine the core losses [34]. In this way, the correct sizing of the transformer parameters enables a reduction of the total losses.

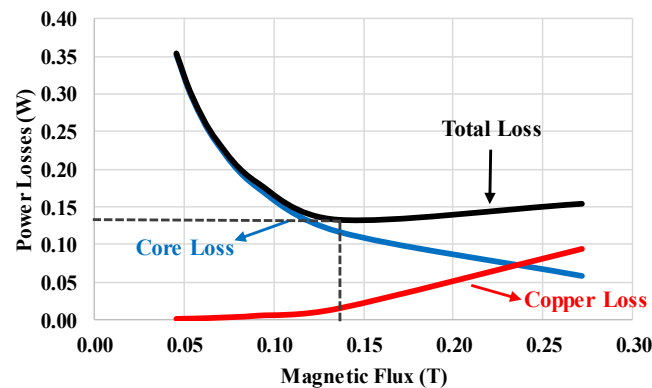


Figure 14. Power losses of the high-frequency power transformer.

Considering the high-frequency transformer, it is necessary to take into account the skin effect. Based on Equation (15), it is possible to determine the maximum diameter of the wire for the operating frequency,  $f$ , in order to minimize the skin effect [34]. In addition, considering several wires with smaller sections makes them more malleable, allowing them to be wound up in the shape of the transformer in an easier and more precise way. Thus, taking into account a current density of 3 A/mm<sup>2</sup> and the AWG #26 copper wire existing at the laboratory, it is possible to size the number of required parallel wires for each winding.

$$D_{AWG} = \frac{6.62}{\sqrt{f}} \times 2 \quad (15)$$

The copper loss is determined by the square of the current, and the internal resistance of the winding  $R_W$ . The  $R_W$  is proportional to the resistivity,  $\rho$ , the mean length turns,  $MLT$ , and the number of turns,  $N$ , and inversely proportional to the section area,  $A_s$ , as shown in Equation (16) [34].

$$R_W = \frac{\rho MLT N}{A_s} \quad (16)$$

The number of turns,  $N$ , also influences the change in flux,  $\Delta B$ , as presented in Equation (17), which is proportional to the flux,  $\lambda_1$ , and inversely proportional to the effective cross-section of the core,  $A_c$  [34].

$$\Delta B = \frac{\lambda_1}{2 N A_c} 10^4 \quad (17)$$

The flux,  $\lambda_1$ , represents the volt-seconds applied to the primary winding of the high-frequency transformer and is directly proportional to the input voltage,  $v_{in}$ , the duty cycle,  $D$ , and inversely proportional to the frequency,  $f$ , shown in Equation (18) [34].

$$\lambda_1 = V_{in} D \left( \frac{1}{f} \right) \quad (18)$$

The core losses,  $P_c$ , as it is possible to see, in Equation (19), depend on the operating frequency,  $f$ , the alternating current flux density,  $B_{ac}$ , the core weight of the transformer,  $W_{tfe}$ , and some intrinsic core loss coefficients,  $k$ ,  $m$  and  $n$  [34].

$$P_c = k(f)^m (B_{ac})^n W_{tfe} 10^{-3} \quad (19)$$

For sizing correctly the high-frequency transformer, all the previously stated constraints that influence the transformer sizing are considered. An ETD 59 ferrite core is chosen, which has a maximum magnetic flux density close to 320 mT and an effective cross-sectional area of 3.677 cm<sup>2</sup>. After some calculations, it is concluded that in order to minimize the total power losses, the best operation point can be acquired with a magnetic flux close to 136 mT. At these conditions, the total losses of the high-frequency transformer are near 132 mW. In Figure 14, the theoretical power losses of the high-frequency power transformer are presented.

A summary of the values obtained in the design of the high-frequency transformer is given in Table 6.

**Table 6.** Characteristics of the high-frequency transformer windings.

Description	Variables	Primary Side	Secondary Side	Units
Number of turns	$N$	2 + 2	20	-
Required wired section	$A_s$	2.7	0.3	mm <sup>2</sup>
Number of AWG				
#26 conductors in parallel	$nc$	21	2	-
Maximum current	$I_{max}$	8.2	0.82	A

After determining the main characteristics of the high-frequency transformer and respective assembly, a preliminary test was conducted to verify the desired conversion ratio (1:1:10) for a frequency of 100 kHz.

#### 5.4. Mutually Coupled Inductance

In order to perform the connection with the power grid, two mutual coupling coils are used, with one of the windings connected to the phase and the other winding connected to the neutral. This configuration helps mitigating the noise caused by the MOSFET switching devices, which induce high-frequency parasitics of currents and voltages. Additionally, it has the advantage of obtaining an equivalent inductance value four times higher than the individual value of each one, considering that the inductance value of each coil is the same. The inductance value of an inductor,  $L$ , depends on the number of turns,  $N$ , and on parameters related to its construction, such as the cross-section area,  $A$ , the length of the core material,  $l$ , and the permeability of the material,  $\mu_0$ , Equation (20).

$$L = \frac{\mu_0 N^2 A}{l} \quad (20)$$

In Equation (15), it can be seen that if the number of turns ( $N$ ) is duplicated, the inductance value can reach four times its previous value. In this way, and considering that each coil has the same number of turns, the equivalent inductance value of the coils in series should be four times the individual value of each one. The coupling inductor was dimensioned in order to withstand a current of 2 A and has an equivalent inductance of 8 mH. For this, the software EPCOS magnetic design tool was used to determine the number of turns and other constructive parameters to obtain the inductance with desired characteristics. In this work, an ETD 59 ferrite core, similar to that used for the design of the high-frequency transformer, was used. In this way, two windings with 70 turns each, with a conductor wire AWG #15, and an air gap of 1 mm, were implemented.

## 6. Experimental Results

In this section, some experimental results of the microinverter are presented and discussed, validating the topology and the new functionalities.

### 6.1. Validation of the DC–DC Power Converter

The preliminary laboratory tests are focused on the DC–DC power converter, in order to verify experimentally the prototype functionalities. These experimental tests are conducted in order to validate the operation in mode 3 of the multifunctional isolated microinverter, charging the BESS and injecting energy into the power grid. The experimental results of the operation of the DC–DC converter in mode 3 presented in Figure 15 show the operation with a duty cycle of 50%, injecting all the power available from the solar PV module into the power grid. The results are obtained with a Tektronix TPS2024 digital oscilloscope.

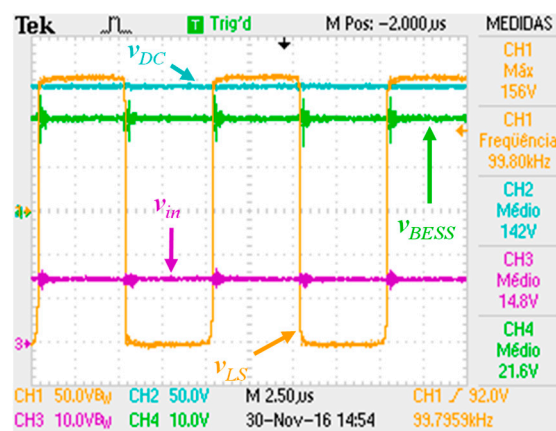


**Figure 15.** Experimental results of the DC–DC power converter: Input voltage ( $v_{in}$ ), BESS voltage ( $v_{BESS}$ ), DC-link voltage ( $v_{DC}$ ) and secondary winding voltage ( $v_{LS}$ ) when the transformer operates with a 50% duty cycle.

When the MPPT algorithm control is activated, the expected magnetic short-circuit of the transformer imposes a null voltage on the primary side of the high-frequency transformer during a short time, as shown in Figure 16a. This figure also shows that the DC–DC power converter operates in current fed mode, and the  $v_{DC}$  increased from 148 V (when the MPPT variable,  $\delta_{MPPT}$ , is disabled) as shown in Figure 15 to 166 V (when  $\delta_{MPPT}$  is enabled). If the time of the magnetic short-circuit increases, the voltage of the primary side of the transformer, and consequently, the drain-source voltage of the MOSFET increases, reaching a value almost four times higher than the input voltage, as can be seen in Figure 16b.

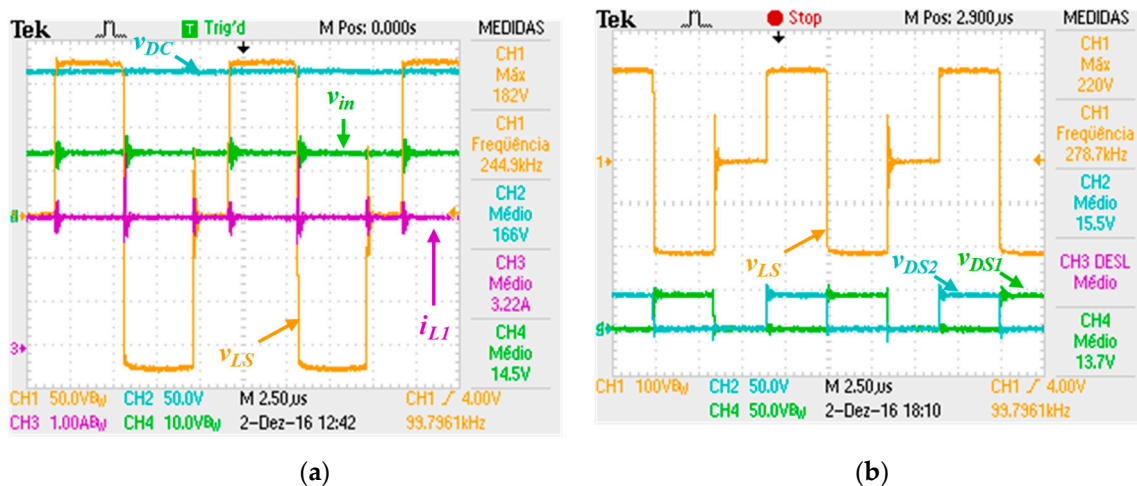


**Figure 16.** Experimental results of the DC–DC power converter: (a)  $v_{DC}$ ,  $v_{in}$ ,  $v_{LS}$  and inductor current ( $i_{L1}$ ) with the MPPT algorithm enabled; (b)  $v_{LS}$  and the drain-source voltage ( $v_{DS1}$  and  $v_{DS2}$ ) in each MOSFET with the MPPT algorithm enabled.

When the BESS control algorithm is activated, the DC–DC power converter starts to charge the BESS, injecting the surplus energy from the solar PV module into the PG, as can be seen in the experimental results shown in Figure 17. In the first instant represented, it can be verified that the BESS, and implicitly  $C_3$ , are charged by the solar PV module. This period of BESS charge is imposed by the BESS control variable,  $\delta_{BESS}$ , increasing the BESS current,  $i_{BESS}$ , during a certain period of time. The voltage induced in the secondary winding of the transformer, where the energy at this moment is injected into the power grid (time interval represented in Figure 17 as PG) can also be seen. Finally, a magnetic short-circuit to the transformer’s primary windings is created, where the energy from PV is stored in  $L_1$ , repeating the process once again. This last period is imposed by the MPPT control algorithm variable,  $\delta_{MPPT}$ , as can be seen in Figure 17. In these three last states,  $C_3$  is responsible for filtering the current ripple and maintaining a constant BESS current. At this point, it was possible to validate the principle of operation of the proposed topology as well as the proposed control algorithm, proving the versatility of the solution presented.

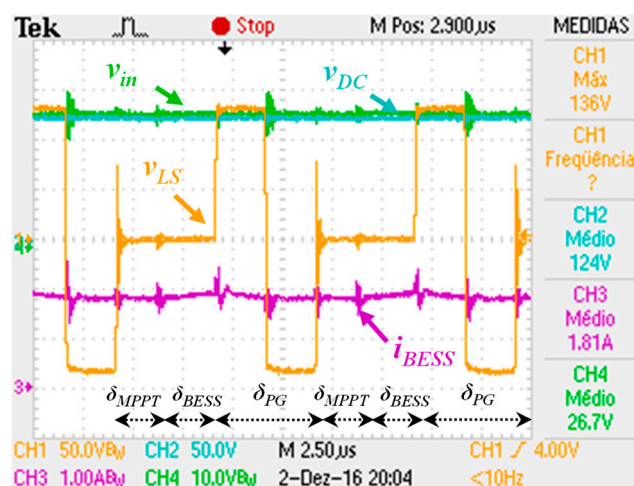


**Figure 17.** Experimental results of the DC–DC power converter:  $v_{DC}$ ,  $v_{in}$ ,  $v_{LS}$  and  $i_{L1}$  with the MPPT and the BESS control algorithms enabled.

## 6.2. Multifunctional Isolated Microinverter Operation

After the validation of each power converter and each control algorithm, the multifunctional isolated microinverter in full operation is validated, particularly the DC-link voltage control algorithm. For the DC–AC power converter and for steady-state operation, the results were obtained with a Yokogawa DL708e digital oscilloscope.

Firstly, it is necessary to charge the BESS with a specific control algorithm: the experimental result exposed in Figure 18. The BESS control algorithm consists of charging the BESS with a constant current of 3 A until the voltage reaches the nominal value. Once it reaches this value, the algorithm changes to a constant voltage charge control. However, as the measuring equipment only allows a maximum time storage of 480 s, Figure 18 only shows the first 450 s of the charging process.

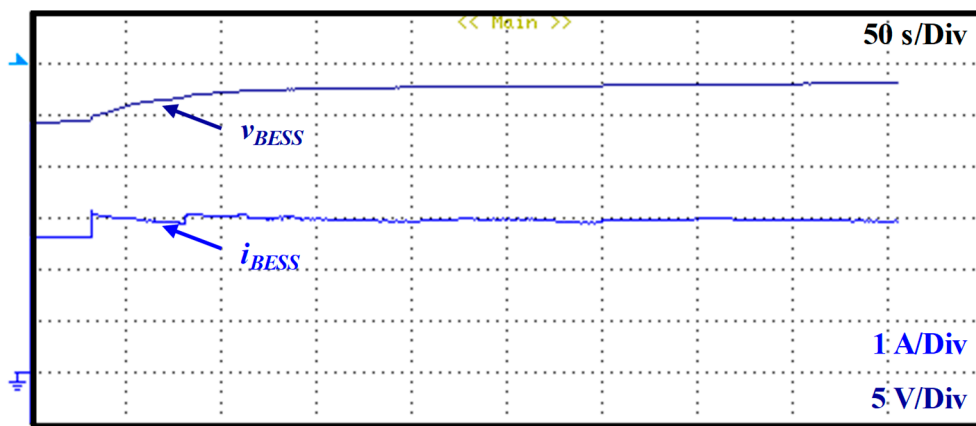


**Figure 18.** Experimental results of the developed multifunctional isolated microinverter: Voltage ( $v_{BESS}$ ) and current ( $i_{BESS}$ ) of the BESS during the charging process.

Once the BESS is fully charged, the available energy is injected into the PG. For safety reasons, an isolation transformer with a turns ratio of 230:40 was used in order to create a lower voltage power grid during the experimental tests. A DC-link voltage reference of 80 V and an AC current with 1 A peak were defined in this test. The results are presented in Figure 19, the current produced by the DC–AC power converter being visible, which is almost sinusoidal with 1 A peak and with a phase-angle of  $180^\circ$  related to the power grid voltage. Additionally, it was possible to see the correct regulation of the DC-link, where a stable voltage of around 80 V was maintained. By using a Fluke 435 power quality analyzer, it was possible to verify that the AC current produced by the developed multifunctional isolated microinverter had a total harmonic distortion (THD) lower than 2%, even with a power grid voltage presenting a THD of approximately 4%.

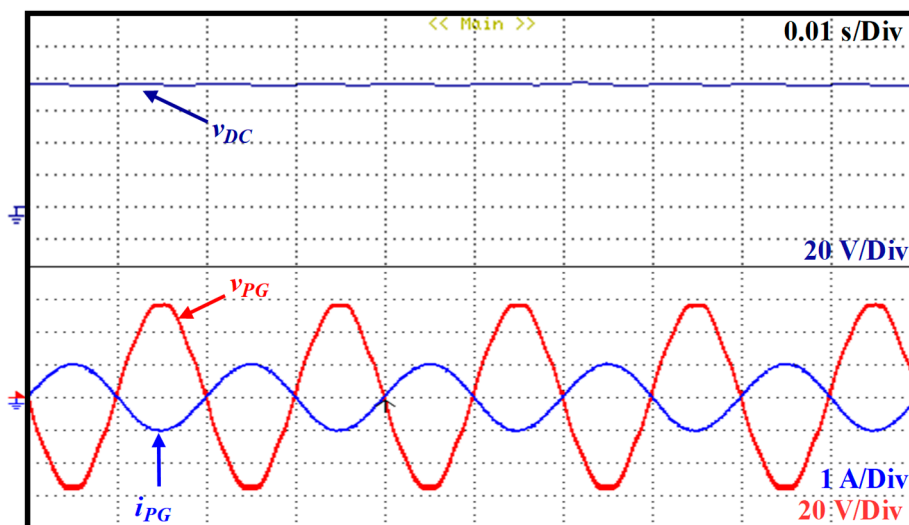


**Figure 19.** Experimental results of the developed multifunctional isolated microinverter: oltage at the DC-link ( $v_{DC}$ ), voltage ( $v_{PG}$ ) and current ( $i_{PG}$ ) on the power grid.

## 7. Conclusions

In this paper, a novel multifunctional topology for isolated microinverter applications is presented. The proposed topology consists of a DC–DC power converter followed by a DC–AC power converter, and it is able to inject the power produced by a solar photovoltaic (PV) module into the power grid and/or to charge a battery energy storage system (BESS). The DC–DC power converter is responsible for extracting the maximum power available from the solar PV module, and using it to store energy in the BESS or to inject energy into the PG through the DC–AC converter. The principle of operation is explained in detail and confirmed by simulation and experimental results achieved with a developed laboratory prototype. The versatility of the proposed multifunctional isolated microinverter is demonstrated in several operation modes, namely when performing BESS charging with the conventional constant current followed by constant voltage algorithm, and at the same time, injecting the remaining power into the PG.

Highlighting the main scientific contributions, and compared with conventional microinverters, the proposed topology allows the interface of a solar PV module with the power grid and with a BESS. This feature allows the user to be a prosumer, producing and consuming their own energy, even during lower production hours. Compared to emerging microinverters with similar functionalities, the proposed topology does not require the insertion of a third energy conversion stage dedicated exclusively to the interface with a BESS. With the proposed configuration, control algorithm, and by using a lower number of fully-controlled switching devices, it is possible to obtain a more compact system. Despite giving up the dedicated stage to interface with BESS, the multifunctional topology guarantees a fully dedicated charging mode to charge the BESS.

During the experimental tests, it was found that the best convergence results of the maximum power point (MPP) were obtained when maintaining high sampling frequencies and low updating times of the maximum power point tracker (MPPT) control variable together with a sliding average. In this way, it is possible to mitigate the noise in the measured solar PV voltage and current, that cause instabilities in the MPPT algorithm.

As further work, all the microinverter printed circuit boards and components will be redesigned in order to achieve a more compact and reliable version of the prototype to be tested in real operating conditions, outside the laboratory. Furthermore, the use of higher-order coupling filters will be investigated, such as the LCL, in order to reduce the component size. Additionally, it could be interesting to investigate other advanced control methods to improve the system performance, as well as the integration of a planar power transformer.

**Author Contributions:** L.A.M.B. led the investigation and experimental validation under the supervision of J.G.P.; M.T. participated in the design of the hardware prototype, sizing components and design of the predictive current control; T.J.C.S. participated in the hardware prototype development and design of the SPWM modulation technique; J.L.A. participated in the development of microinverter control algorithms as well as in the sizing of components. All authors have read and agreed to the published version of the manuscript.

**Funding:** This work has been supported by FCT—Fundação para a Ciência e Tecnologia within the R&D Units Project Scope: UIDB/00319/2020. This work has been supported by the FCT Project QUALITY4POWER PTDC/EEI-EEE/28813/2017. Luis A. M. Barros is supported by the doctoral scholarship PD/BD/143006/2018 granted by the Portuguese FCT foundation. Mohamed Tanta was supported by FCT PhD grant with a reference PD/BD/127815/2016 granted by the Portuguese FCT agency. Tiago J. C. Sousa is supported by the doctoral scholarship SFRH/BD/134353/2017 granted by the Portuguese FCT agency.

**Conflicts of Interest:** The authors declare no conflict of interests.

## References

1. Humada, A.M.; Samsuri, F.B.; Hojabria, M.; Mohamed, M.B.; Sulaiman, M.H.B.; Dakheel, T.H. Modeling of photovoltaic solar array under different levels of partial shadow conditions. In Proceedings of the Power Electronics and Motion Control Conference and Exposition (PEMC), 2014 16th International, Antalya, Turkey, 21–24 September 2014; pp. 461–465. [\[CrossRef\]](#)
2. Luque, A.; Hegedus, S. (Eds.) *Handbook of Photovoltaic Science and Engineering*; John Wiley & Sons: Hoboken, NJ, USA, 2011; ISBN 978-0-470-72169-8.
3. Ruiz-Caballero, D.A.; Barbi, I. A new flyback-current-fed push-pull DC-DC converter. *IEEE Trans. Power Electron.* **1999**, *14*, 1056–1064. [\[CrossRef\]](#)
4. Nanakos, A.C.; Christidis, G.C.; Tatakis, E.C. Weighted efficiency optimization of flyback microinverter under improved boundary conduction mode (i-BCM). *IEEE Trans. Power Electron.* **2015**, *30*, 5548–5564. [\[CrossRef\]](#)
5. Felgemacher, C.; Jaeger, P.; Kobeissi, A.; Pfeiffer, J.; Wiegand, D.; Kruschel, W.; Dombert, B.; Araujo, S.V.; Zacharias, P. Design of photovoltaic microinverter for off-grid and grid-parallel applications. In Proceedings of the Integrated Power Systems (CIPS), 2014 8th International Conference, Nuremberg, Germany, 25–27 February 2014; pp. 1–6, ISBN 978-3-8007-3578-5.
6. Gazoli, J.R.; Villalva, M.G.; Siqueira, T.G.; Ruppert, E. Micro-inverter for integrated grid-tie PV module using resonant controller. In Proceedings of the 2012 IEEE Power and Energy Society General Meeting, San Diego, CA, USA, 22–26 July 2012; pp. 1–8. [\[CrossRef\]](#)
7. Cao, D.; Jiang, S.; Peng, F.Z.; Li, Y. Low cost transformer isolated boost half-bridge micro-inverter for single-phase grid-connected photovoltaic system. In Proceedings of the 2012 Twenty-Seventh Annual IEEE Applied Power Electronics Conference and Exposition (APEC), Orlando, FL, USA, 5–9 February 2012; pp. 71–78. [\[CrossRef\]](#)
8. Choi, Y.-G.; Lee, H.-S.; Kang, B.; Lee, S.-C.; Yoon, S.-J. Compact Single-Stage Micro-Inverter with Advanced Control Schemes for Photovoltaic Systems. *Energies* **2019**, *12*, 1234. [\[CrossRef\]](#)
9. Zhang, F.; Xie, Y.; Hu, Y.; Chen, G.; Wang, X. A Hybrid Boost-Flyback/Flyback Microinverter for Photovoltaic Applications. *IEEE Trans. Ind. Electron.* **2019**, *67*, 308–318. [\[CrossRef\]](#)
10. Lodh, T.; Pragallapati, N.; Agarwal, V. Novel control scheme for an interleaved flyback converter based solar PV microinverter to achieve high efficiency. *IEEE Trans. Ind. Appl.* **2018**, *54*, 3473–3482. [\[CrossRef\]](#)
11. Watanabe, H.; Itoh, J.; Koike, N.; Nagai, S. PV Micro-inverter topology using LLC resonant converter. *Energies* **2019**, *12*, 3106. [\[CrossRef\]](#)
12. Tayebi, S.M.; Hu, H.; Batarseh, I. Advanced DC-Link Voltage Regulation and Capacitor Optimization for Three-Phase Microinverters. *IEEE Trans. Ind. Electron.* **2018**, *66*, 307–317. [\[CrossRef\]](#)
13. Rajeev, M.; Agarwal, V. Analysis and Control of a Novel Transformer-Less Microinverter for PV-Grid Interface. *IEEE J. Photovolt.* **2018**, *8*, 1110–1118. [\[CrossRef\]](#)
14. Roy, J.; Xia, Y.; Ayyanar, R. High step-up transformerless inverter for AC module applications with active power decoupling. *IEEE Trans. Ind. Electron.* **2018**, *66*, 3891–3901. [\[CrossRef\]](#)
15. Abedeen, E.; Gaafar, M.; Orabi, M.; Sheir, A.; Youssef, M. A Novel Dual-Input High-Gain Transformer-less Multi-Level Single-Phase Micro-inverter for PV systems. *IEEE Trans. Power Electron.* **2019**. [\[CrossRef\]](#)

16. Yuan, J.; Blaabjerg, F.; Yang, Y.; Sangwongwanich, A.; Shen, Y. An Overview of Photovoltaic Microinverters: Topology, Efficiency, and Reliability. In Proceedings of the 2019 IEEE 13th International Conference on Compatibility, Power Electronics and Power Engineering (CPE-POWERENG), Sonderborg, Denmark, 23–25 April 2019; pp. 1–6. [\[CrossRef\]](#)
17. Alluhaybi, K.; Batarseh, I. Review and Comparison of Single-Phase Grid-Tied Photovoltaic Microinverters. In Proceedings of the 2018 IEEE Energy Conversion Congress and Exposition (ECCE), Portland, OR, USA, 23–27 September 2018; pp. 7101–7108. [\[CrossRef\]](#)
18. Hasan, R.; Mekhilef, S.; Seyedmahmoudian, M.; Horan, B. Grid-connected isolated PV microinverters: A review. *Renew. Sustain. Energy Rev.* **2017**, *67*, 1065–1080. [\[CrossRef\]](#)
19. Poshtkouhi, S.; Fard, M.; Hussein, H.; Santos, L.M.D.; Trescases, O.; Varlan, M.; Lipan, T. A dual-active-bridge based bi-directional micro-inverter with integrated short-term li-ion ultra-capacitor storage and active power smoothing for modular pv systems. In Proceedings of the 2014 Twenty-Ninth Annual IEEE Applied Power Electronics Conference and Exposition (APEC), Fort Worth, TX, USA, 16–20 March 2014; pp. 643–649. [\[CrossRef\]](#)
20. Vera, F.A.M.; Prado, J.D.P.; Moriano, J.J.S.; Zuñiga, C.G.P.; Rosas Celi, D.E.S.y. Bidirectional multiport microinverter and grid-multimode-operation control for a non-linear load. In Proceedings of the 2017 IEEE Workshop on Power Electronics and Power Quality Applications (PEPQA), Bogota, Colombia, 31 May–2 June 2017; pp. 1–6. [\[CrossRef\]](#)
21. Lodh, T.; Agarwal, V. Single stage multi-port Flyback type solar PV module integrated micro-inverter with battery backup. In Proceedings of the 2016 IEEE International Conference on Power Electronics, Drives and Energy Systems (PEDES), Trivandrum, India, 14–17 December 2016; pp. 1–6. [\[CrossRef\]](#)
22. Patel, H.; Agarwal, V. MATLAB-based modeling to study the effects of partial shading on PV array characteristics. *IEEE Trans. Energy Convers.* **2008**, *23*, 302–310. [\[CrossRef\]](#)
23. Esram, T.; Chapman, P.L. Comparison of photovoltaic array maximum power point tracking techniques. *IEEE Trans. Energy Convers.* **2007**, *22*, 439–449. [\[CrossRef\]](#)
24. Femia, N.; Petrone, G.; Spagnuolo, G.; Vitelli, M. Optimization of perturb and observe maximum power point tracking method. *IEEE Trans. Power Electron.* **2005**, *20*, 963–973. [\[CrossRef\]](#)
25. Buchman, I. *Batteries in a Portable World: A Handbook on Rechargeable Batteries for Non-Engineers*, 3rd ed.; Cadex Electronics Inc.: Richmond, VA, USA, 2011.
26. Pinto, J.; Monteiro, V.; Gonçalves, H.; Afonso, J.L. Onboard reconfigurable battery charger for electric vehicles with traction-to-auxiliary mode. *IEEE Trans. Veh. Technol.* **2014**, *63*, 1104–1116. [\[CrossRef\]](#)
27. Karimi-Ghartemani, M.; Iravani, M.R. A method for synchronization of power electronic converters in polluted and variable-frequency environments. *IEEE Trans. Power Syst.* **2004**, *19*, 1263–1270. [\[CrossRef\]](#)
28. Timbus, A.; Liserre, M.; Teodorescu, R.; Rodriguez, P.; Blaabjerg, F. Evaluation of current controllers for distributed power generation systems. *IEEE Trans. Power Electron.* **2009**, *24*, 654–664. [\[CrossRef\]](#)
29. Buso, S.; Malesani, L.; Mattavelli, P. Comparison of current control techniques for active filter applications. *IEEE Trans. Ind. Electron.* **1998**, *45*, 722–729. [\[CrossRef\]](#)
30. Pinto, J.G.O.; Macedo, R.; Monteiro, V.; Barros, L.; Sousa, T.; Afonso, J.L. Single-phase shunt active power filter based on a 5-level converter topology. *Energies* **2018**, *11*, 1019. [\[CrossRef\]](#)
31. Tanta, M.; Pinto, J.; Monteiro, V.; Martins, A.P.; Carvalho, A.S.; Afonso, J.L. Deadbeat Predictive Current Control for Circulating Currents Reduction in a Modular Multilevel Converter Based Rail Power Conditioner. *Appl. Sci.* **2020**, *10*, 1849. [\[CrossRef\]](#)
32. Chen, M.; Rincon-Mora, G.A. Accurate electrical battery model capable of predicting runtime and IV performance. *IEEE Trans. Energy Convers.* **2006**, *21*, 504–511. [\[CrossRef\]](#)
33. Pena-Alzola, R.; Liserre, M.; Blaabjerg, F.; Ordonez, M.; Yang, Y. LCL-filter design for robust active damping in grid-connected converters. *IEEE Trans. Ind. Inform.* **2014**, *10*, 2192–2203. [\[CrossRef\]](#)
34. McLyman, C.W.T. *Transformer and Inductor Design Handbook*; CRC Press: Boca Raton, FL, USA, 2016; ISBN 0-8247-5393-3.

